Biocompatible Pressure Sensing Skins for Minimally Invasive Surgical Instruments

Veaceslav Arabagi, Ouajdi Felfoul, Andrew H. Gosline, *Member, IEEE*, Robert J. Wood, *Member, IEEE*, and Pierre E. Dupont, *Fellow, IEEE*

***Abstract*— This paper presents 800-μm thick, biocompatible sensing skins composed of arrays of pressure sensors. The arrays can be configured to conform to the surface of medical instruments so as to act as disposable sensing skins. In particular, the fabrication of cylindrical geometries is considered here for use on endoscopes. The sensing technology is based on polydimethylsiloxane synthetic silicone encapsulated microchannels filled with a biocompatible salt-saturated glycerol solution, functioning as the conductive medium. A multi-layer manufacturing approach is introduced that enables stacking sensing microchannels, mechanical stress concentration features, and electrical routing via flexcircuits in a thickness of less than 1 mm. The proposed approach is inexpensive and does not require clean room tools or techniques. The mechanical stress concentration features are implemented using a patterned copper layer that serves to improve sensing range and sensitivity. Sensor performance is demonstrated experimentally using a sensing skin mounted on a neuroendoscope insertion cannula and is shown to outperform previously developed non-biocompatible sensors.**

***Index Terms*— Pressure sensing arrays, sensing skins, surgical instruments, biocompatible sensors.**

I. Introduction

THERE ARE substantial benefits to minimally invasive surgery including reduced collateral tissue damage, faster recovery and decreased health care costs [1]. A major shortcoming, however, is the reduced situational awareness experienced by the clinician in comparison with open surgery. This is caused by an almost exclusive reliance on imaging (e.g., optical, ultrasound) to substitute for exteroceptive sensing, i.e., sensing interaction with surrounding tissues. Image-based estimates of tissue deformation must be used to infer contact and to crudely assess the magnitude of the applied force. This approach works best for simple procedures and when high-quality real-time imaging of the entire surgical field is possible, e.g., laparoscopy. The lack of force/tactile sensing can lead to the inadvertent application of excess or insufficient force resulting in tissue damage and/or inferior procedural outcomes [2].

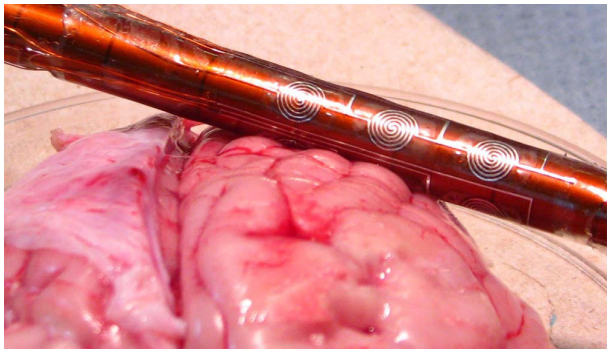

Fig. 1. Neuroendoscopic sheath with eGaIn pressure sensor array being tested on an *ex vivo* sheep brain [24].

To address these issues, the incorporation of force sensing has been a longstanding goal for handheld and robotic laparoscopic instruments [3]. However, many approaches considered to date pose challenges with regard to size, biocompatibility and bendable radius of curvature [4].

Recently, there has been a significant amount of work on the development of thin sensor arrays. Small, implantable sensors for measuring intraocular pressures have been proposed based on differential pressure [5] and capacitive sensing [6]–[8]. Various techniques employing stretchable electronics [9], pressure sensitive transistor [10], and piezo-phototronics arrays [11], [12] exist for tactile sensing in the form of artificial skin, however they all employ expensive lithographic equipment and clean room techniques. As inexpensive alternatives, soft sensors containing microchannels filled with both conductive (doped) polymers [13], as well as conductive liquids [14]–[20] were developed. Primarily these sensors have been used to measure strain induced by stretching, however they have also been adapted to sense curvature [21], shear forces [22] and catheter port pressure [23]. This technology is simple and inexpensive and so seems promising for biomedical applications.

These soft sensors are comprised of submillimeter channels filled with conductive fluid embedded inside a PDMS (polydimethylsiloxane synthetic silicone) sheet whose resistance changes under physical deformation. In prior work, we presented a method for creating contact pressure sensor arrays of cylindrical geometry and also demonstrated that they possessed sufficient sensitivity and range for measuring

Manuscript received August 12, 2015; revised October 20, 2015; accepted October 25, 2015. Date of publication November 5, 2015; date of current version February 4, 2016. This work was supported in part by the National Institutes of Health under Grant R01HL124020 and in part by the Wyss Institute for Biologically Inspired Engineering. The associate editor coordinating the review of this paper and approving it for publication was Prof. Ravinder S. Dahiya.

V. Arabagi was with Boston Children's Hospital, Harvard Medical School, Boston, MA 02115 USA. He is now with Helbling Precision Engineering, Cambridge, MA 02142 USA (e-mail: badeaslava@gmail.com).

O. Felfoul was with Boston Children's Hospital, Harvard Medical School, Boston, MA 02115 USA. He is now with GE Healthcare, Waukesha, WI 53188 USA (e-mail: ouajdi.felfoul@gmail.com).

A. H. Gosline was with Boston Children's Hospital, Harvard Medical School, Boston, MA 02115 USA. He is now with Human Design Medical LLC, Charlottesville, VA 22902 USA (e-mail: andrewgosline@gmail.com).

R. J. Wood is with the School of Engineering and Applied Sciences, Wyss Institute, Harvard University, Cambridge, MA 02138 USA (e-mail: rjwood@eecs.harvard.edu).

P. E. Dupont is with Boston Children's Hospital, Harvard Medical School, Boston, MA 02115 USA (e-mail: pierre.dupont@childrens.harvard.edu).

Digital Object Identifier 10.1109/JSEN.2015.2498481

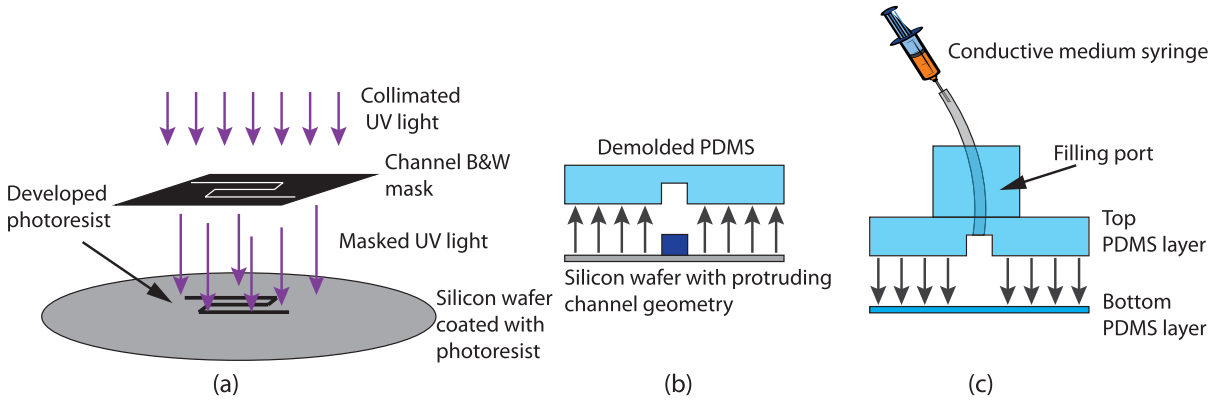

Fig. 2. Manufacturing steps for the soft sensing skin: (a) A photolithography process is used to pattern extrusions of SU-8 photoresist on a silicon wafer, representing the spiral pattern; (b) PDMS is spun on the silicon wafer with the protruding geometry, creating a spiral channel after demolding; (c) The channel is sealed by bonding it to a flat PDMS bottom layer and later a conductive medium is injected through a filling port. Modified from [24].

clinically-relevant pressures during neuroendoscopy [24]. The goal of [24] was to provide a means to automatically monitor contact pressures over the surface of a neuroendoscope inserted inside the brain (see Fig. 1) and to alert the clinician, whose attention would be focused on the endoscope's tip, if lateral scope motion induced tissue-damaging pressures. Since the brain is among the most delicate tissues in the body, this represents an extreme test of sensing capabilities compared to most applications throughout the body.

The sensors developed in this prior work used a liquid metal, eutectic Gallium Indium (eGaIn), as the conductive medium, rendering them non-biocompatible. As an alternative, ionic aqueous solutions have been previously employed in [18], [19], [23], however since siloxane-based polymers, such as PDMS, are highly permeable to water vapor, the overall thickness of these sensors is forced to be large so as to reduce the water evaporation rate. Surface treatments, such as Parylene C, to reduce permeability have been considered [25], however, these techniques increase the cost and complexity of fabrication. As an alternative solution, we propose an ionic solution composed of glycerol saturated with NaCl. Since a salt saturated solution of glycerol contains significantly fewer ions that an aqueous solution, its resistance is higher. Thus, the design challenge with this approach is to achieve sufficiently high sensitivity and signal to noise ratio.

The contribution of this paper is to demonstrate a flexible biocompatible cylindrically-packaged sensor array that provides improved accuracy over previous non-biocompatible sensor arrays [24]. The next section describes sensor design and manufacturing, introducing stacked multi-lamina construction and a mechanical amplification technique. In Section III, an experimental evaluation of the mechanical stress concentration layer is presented to demonstrate the efficacy of the approach. Section IV provides an experimental comparison of the proposed approach with our prior non-biocompatible eGaIn sensors in the context of a sensing skin for a neurosurgical endoscope [24]. Conclusions appear in the final section of the paper.

II. Sensor Design and Fabrication

Sensor manufacturing is based on a micro-molding technique illustrated in Fig. 2 [15]. A photolithography process is used to pattern SU-8 extrusions on a Si wafer, serving as the positive channel molds. Next, a spun layer of PDMS is molded onto these features retaining the channel geometry when demolded. These channels are sealed with a flat bottom PDMS layer and filled with an electrically conductive medium through a syringe. When these channels are deformed due to applied pressure, as shown in Fig. 3, the cross section of the channels are reduced resulting in an increase in resistance along the channel.

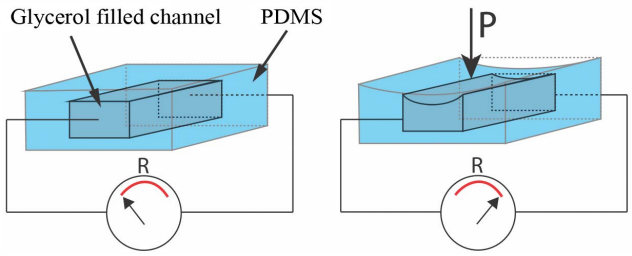

Fig. 3. Sensor operation. Pressure applied to the sensor causes the channel to partially collapse and reduce in cross section. This results in an increase in electrical resistance along the channel. Modified from [24].

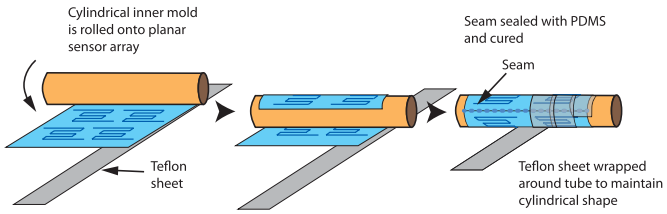

Fig. 4. Fabrication of cylindrical skin. The planar sensor array is rolled onto a flexible polymer tube, the seam is sealed with PDMS and the fabrication is maintained in its cylindrical shape using Teflon. The Teflon is removed once the PDMS is cured.

To obtain a cylindrical geometry, the planar array of sensors is mounted on a substrate tube as shown in Fig. 4. Since the sensor array itself is 800μm thick and flexible, the substrate tube material and thickness can be selected, according to the application, to achieve the desired overall stiffness properties of the sensing skin.

A. Electrical Circuit

Since a DC current causes charge separation in an ionic solution, a zero-mean square wave generating circuit was built

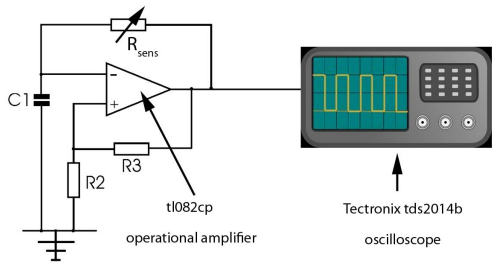

Fig. 5. Schematic of the square wave driving sensor circuit.

to drive the sensors as shown in Fig. 5. Using a sensing channel as a resistor in the circuit, namely R_{sens}, the period of the output square wave is:

$$T = 2R_{sens}C1\lambda, \tag{1}$$

where λ is a constant function of $\{R2, R3\}$. The period varies with sensed normal load. The input frequency of the driving wave must be high enough to avoid charge separation, but not so high as to induce increased conductivity, i.e., in the range of 40Hz to 10MHz [18]. In the experiments reported here, the circuit was tuned to produce a base 1 kHz square wave.

A 500MHz oscilloscope (Tectronix tbs1052b, Beaverton, OR) was used to measure wave period. A Matlab script logged wave period and simultaneous weight scale measurements to a data file at a rate of 5Hz. This is appropriate for our sensor characterization experiments. Alternate faster methods are possible, such as routing the output square wave to a digital counter, as in [19].

B. Stress Concentration Features

As a means of increasing sensitivity for a given applied pressure, stiff inclusions can be introduced in the polymer skin above or below the conductive channel. These features concentrate the stress on the channel and so produce larger channel collapse than would otherwise occur. For example, the curvature sensors of [21] used PDMS columns directly under the sensing channel. This approach is relatively ineffective for measuring normal pressure, however, due to the compliance of PDMS. The approach introduced here, depicted in Fig. 6, utilizes a 100μm-tall copper layer to produce a desired pattern of stress concentrations on the conductive channels. As shown in Fig. 6(b), copper ridges running perpendicular to the sensing channel allows for local pinching of the channel, thus improving sensitivity at a given pressure.

Note that while a separate layer is used here to enable independent control of patterning variables, such features, once optimized, can be directly incorporated into the flex circuit layer described below.

C. Electrical Flex Circuit

To minimize sensor thickness and eliminate manual wiring during manufacturing, a patterned copper clad Kapton film (Pyralux AC, Dupont, Wilmington, DE) was employed as an electrical circuit. The film consists of 12μm copper bonded to a 25μm Kapton substrate and serves to route electrical signals,

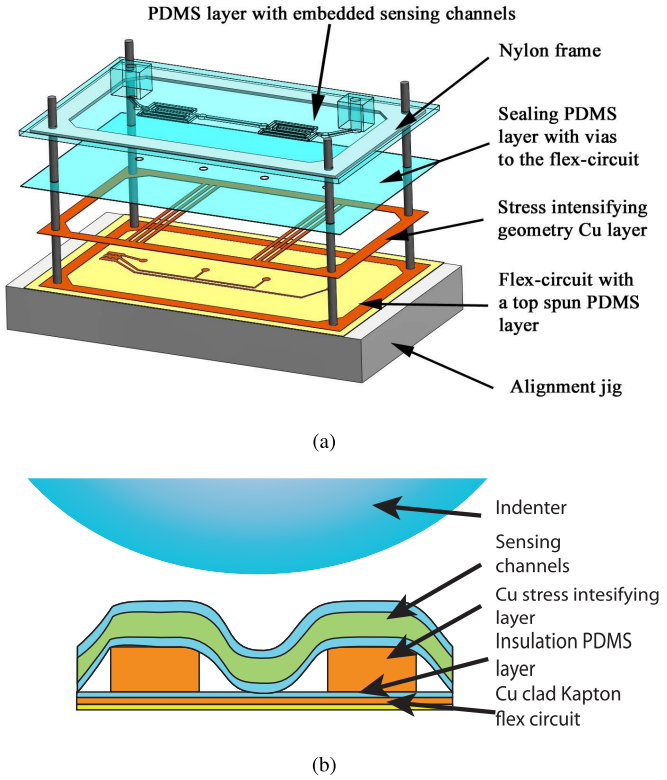

Fig. 6. Sensor schematics: (a) separate layers during the pin alignment step and (b) sensor cross-section illustrating the nominal deformation of the sensing channels due to the stress amplifying layer.

connect neighboring sensors, and provide solder pads for external wiring. The flex circuit is manufactured through a masking and chemical etching technique. In particular, the conducting traces are masked with black ink using a solid ink printer (Xerox ColorQube 8570) and etched in a solution of FeCl until the unmasked copper is dissolved. A sample resulting circuit with included alignment pin holes to streamline the manufacturing process is shown in Fig. 6. Furthermore, electrically connecting individual sensors by copper traces allows their complete sealing, thus eliminating any cross-talk between neighboring sensors due to fluid displacement, a detrimental effect on measurements encountered in [24].

The same manufacturing technique is employed for the stress concentration layer discussed above. A 100μm copper shim is used. Since it has no polymer backing, its underside (unprinted side) is masked with masking tape to preclude etching.

D. Pin Alignment Manufacturing

Each of the layers described above must be aligned with an accuracy of $\sim$1mm. Previously published pin alignment techniques [26] for soft sensors work well for thick layers, but are inadequate for aligning 400μm thick PDMS layers due to a lack of planar rigidity and attractive electrostatic forces between the layers. The solution proposed here is to use a sacrificial fabric cloth that both reinforces the perimeter of the sensor array and contains alignment features. The material needs to be flexible yet not stretchable, as alignment

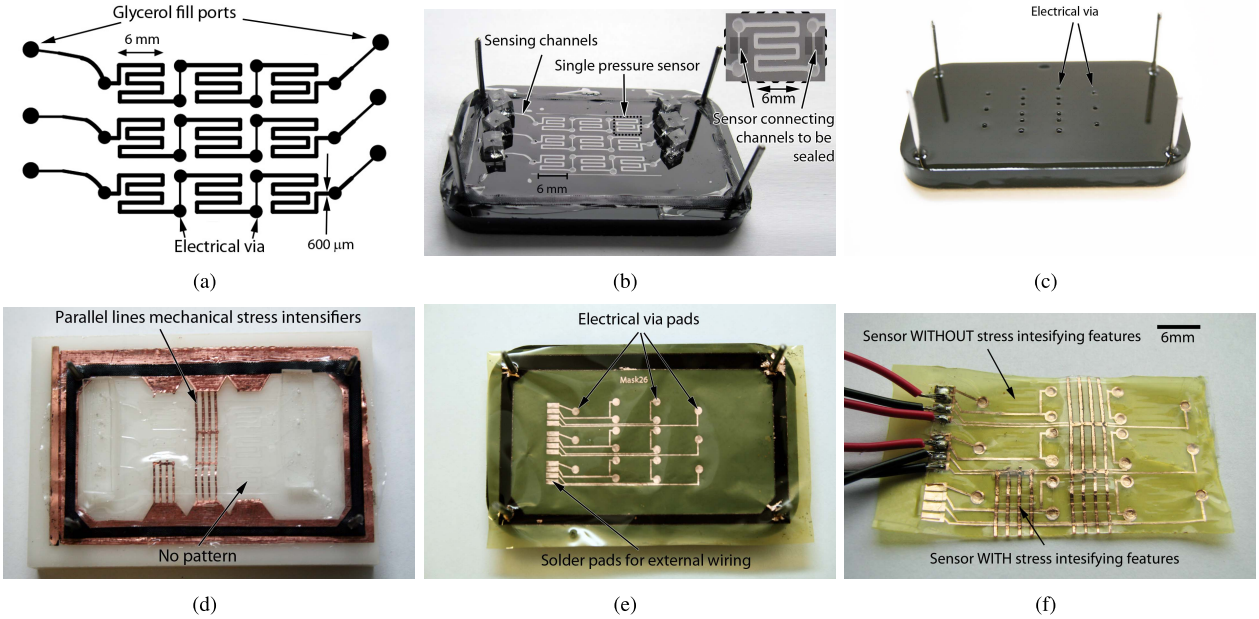

Fig. 7. Sensor layers: (a) photolithography mask showing the geometry and sizing of the sensing channels; (b) top PDMS layer with embedded sensing channels and a nylon cloth frame before demolding; (c) PDMS sealing layer for the sensing channels featuring electrical vias; (d) 100μm thick copper layer, patterned with stress intensifying geometry attached underneath the top sensing layer; (e) flex circuit layer with a spun insulating PDMS layer; and (f) full assembled and deframed multi-layer sensor array featuring sensors with and without stress concentration features.

holes must be geometrically constrained relative to each other. While a rigid frame would be sufficient for alignment, it would preclude peeling of the channel-containing PDMS layer from its Si mold wafer. Ripstop Nylon (0.75 oz. spinnaker cloth) is chosen as the flexible frame due to its excellent in-plane stiffness and porous weave to allow good penetration of PDMS.

E. Biocompatibility

The total layer stack, illustrated in Fig. 6(a), is comprised of four main layers: the PDMS sensing channel layer, the PDMS sealing layer, the stress intensification copper layer, and the copper clad flex circuit. The flex circuit features a 50 μm thick covering PDMS film serving as the electrical insulator, broken only at the via pads, to allow an electrical pathway for the glycerol.

PDMS (silicone) and Kapton (polyimide film) are biocompatible materials that are commonly used in medical devices. Unlike with eGaIn, if the outer PDMS layer is breached during surgery, there is no risk to the patient since glycerol and salt are also biocompatible. Copper, like most metals, can be toxic, but is commonly used in medical devices (e.g., as a conductor). In such applications, and as done in this design, it is embedded in biocompatible materials to avoid direct contact with tissue. Thus, the overall sensor design is biocompatible.

F. Multi-Layer Fabrication Example

The manufacturing process is illustrated here with the fabrication of a 3 $\times$ 3 sensor array as shown in Fig. 7. Each sensor covers a 6 $\times$ 6mm square. The conductive channels comprising each sensor have a rectangular cross section 500μm wide and 100μm high with 600μm separation between neighboring channels. Note that the square sensor geometry was used instead of the prior spiral geometry ([24, Fig. 1]) to maximize the coverage area and to account for the much higher resistance of an ionic fluid compared to a liquid metal.

This sensor design is intended to evaluate the effect of stress concentration features as described in the experiments of the next section. To compare performance with and without stress concentration features, four of the sensors included the features and five did not. The features are comprised of a set of parallel vertical lines (see Fig. 7(d)). Each line is 0.5mm wide, and neighboring lines are separated by 1mm. This feature pattern is intended to maximize resistance change of the channel under normal pressure by balancing the total length of channel that is deformed with the change in channel cross section over the deformed length.

Sensor fabrication relies on three main alignment steps:

1) A silicon wafer is patterned with SU-8 protrusions via the photolithography mask of Fig. 7(a). A ~400μm PDMS layer is spin-coated on a patterned silicon wafer to produce the sensing channels. An alignment Ripstop nylon frame is embedded onto the top layer together with glycerol injection ports, and the layer is vacuum degassed to eliminate any entrapped air. The layer is then cured (Fig. 7(b)) at 80 °C for 15 minutes. A second PDMS layer of ~50μm thickness is spun on an acrylic alignment jig with holes at the electrical vias. The liquid PDMS flows into the jig holes creating cavities that serve to connect the conductive glycerol to the sensing pads on the flex circuit below (Fig. 7(c)). After half curing the via layer at 80 °C for 5 minutes, it is aligned and adhered to the sensing channels.

2) The sealed sensing channels are demolded from the acrylic jig and aligned onto the intensifying geometry layer of 100μm thick, that features a 50μm uncured spun layer of PDMS for adhesion (Fig. 7(d)). The hollow areas of this copper layer need to be free of any residual film or material as they provide a through connection to the flex circuit below. The layers are pressed and cured together.
3) The flex circuit is mounted on an alignment jig (Fig. 7(e)) and spin-coated with a $\sim$200μm thick insulating PDMS layer. The layer is half cured at 80 °C for 5 minutes, after which the electrical pads are manually cleaned from any PDMS residue that would preclude a good electrical connection to the glycerol. The top layers are aligned onto the jig and pressed together. Weights totaling 500g are placed on the entire stack during curing to ensure good adhesion.
4) The salt and glycerol solution is made by mixing 6ml of NaCl in 100ml of 98% glycerol for 12 hours at an elevated temperature of 100 °C without precipitation. The mixture is injected via syringe through the channel fill ports under a microscope. Next, the fill ports are cut out from the sensor array with a blade. Given the low viscosity of the glycerol solution, the channel paths leading up to the fill ports are designed to narrow in width (see Fig. 7(a)) to increase the boundary layer friction effect and so slow its outflow rate. Although some glycerol will flow out, this technique was found effective in maintaining channel pressure prior to sealing and curing. The open channel ends are sealed with PDMS and cured. During the sealing step, the channels connecting neighboring sensors are cut and resealed with PDMS, thus eliminating any cross flow of conducting medium. Finally, the stack is manually cut on the inside of the nylon frame and the sensor array is released (Fig. 7(f)).

To experimentally estimate the resistivity of the salt and glycerol solution, a straight 100 $\times$ 400μm (height $\times$ width) channel was constructed and the output wave period was measured. This test yielded a value of $\approx$16 $\Omega \cdot m$, which can be compared to a value of $\approx$29.4 $\times$ 10^{-8} $\Omega \cdot m$ for eGaIn. The stress concentration features tested experimentally in the next section are intended to boost sensitivity and thus signal-to-noise ratio to compensate for high solution resistivity.

III. Experimental Evaluation of Stress Concentration Feature Effectiveness

Indentation experiments were used to evaluate the stress concentration features. The measurement setup of Fig. 8(a) facilitated repeatable indentation testing. An automated vertical stage was built using a manual micrometer stage powered by a continuous rotation servo and controlled by an Arduino microcontroller.

Pressure sensing is provided by the Scout Pro 200g weight scale (Ohaus Corp., Parsippany, NJ), with data recorded through an RS232 connection in Matlab. A 5mm diameter cylindrical flat tip aluminum indenter was used. The indenter was initialized to be aligned and in contact with the 6 $\times$ 6mm sensing area.

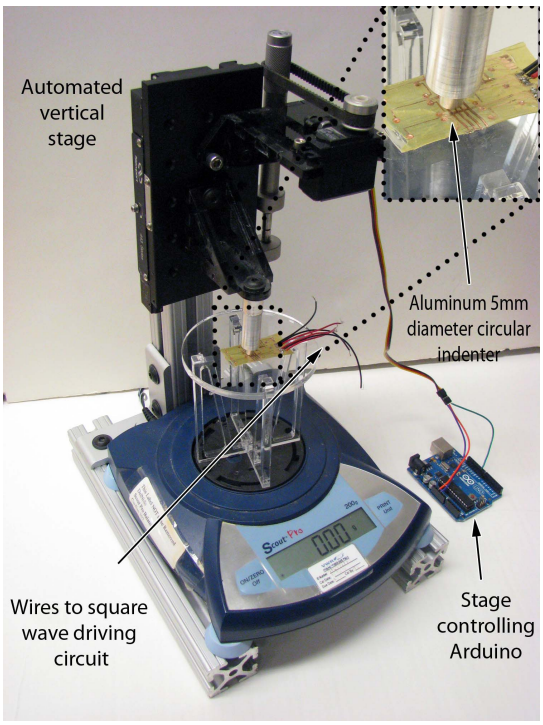

Fig. 8. Experimental setup for automated vertical indenter (top inset portrays a close up of the aluminum indenter).

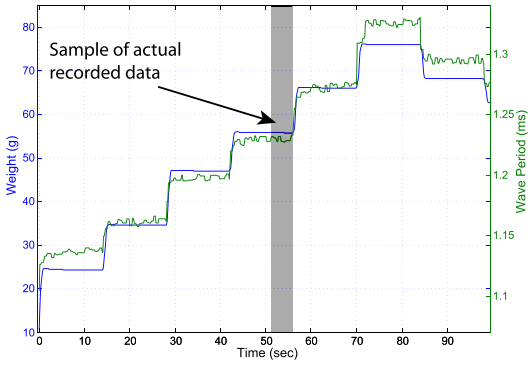

Fig. 9. Sample indentation data performed on a sensor without stress intensifiers. The gray region indicates the width of the window used for for data capture.

Indentation characterization measurements were collected at discrete loads in the following manner: the vertical stage was actuated for a fixed amount of time, then paused, while measurements were recorded, after which the stage was actuated again and the cycle repeated. A typical data set is shown in Fig. 9. To avoid the transient effects immediately after actuation, each load is maintained for 14 sec and the data samples are recorded over the final 4 sec of this period, bounding the recorded data window to the grayed area shown in Fig. 9.

Employing the automated testing setup, the effect of the stress concentration features is presented in Fig. 10. Each data point is given as the mean and standard deviation of

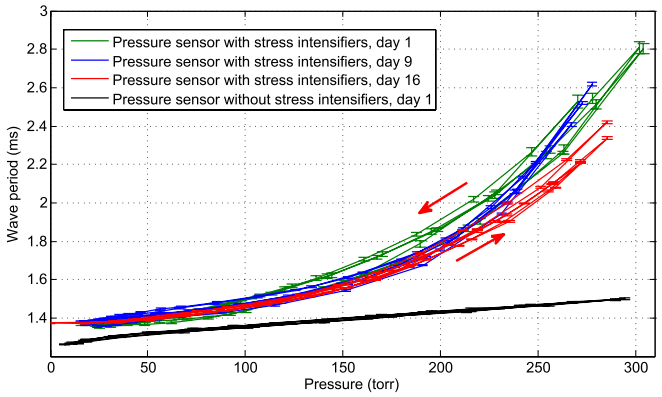

Fig. 10. Indentation results from three loading cycles on sensors with and without stress intensifying features. Mean and standard deviations are computed from last 4 sec of data of each indentation step. Arrows show hysteresis loop directions. For sensor with stress intensifiers, response on days 9 and 16 after manufacturing are also shown.

4 sec of data recorded for a specific stage displacement. Three loading cycles are depicted for sensors with and without stress intensifiers that were collected on the day after sensor fabrication. To evaluate short-term aging, the experiment using the stress-intensifier sensor was repeated nine days and sixteen days after fabrication. These loading cycles are also shown.

The sensor without stress intensifiers exhibits an almost linear and highly-repeatable response in the tested pressure range. This suggests that pressure is being transmitted uniformly to the sensor channels. In contrast, the stress intensifying features provide significant amplification, e.g., an amplification factor of $\sim$1.5 at a pressure of 250torr. This amplification is nonlinear and is likely induced by the large and nonlinear deformations of the channels at their intersection points with the intensifier features. While a small amount of hysteresis can be observed, which may be due to the high viscosity of glycerol, sensor response is repeatable over the three trials.

The Cu electrical pads were observed to oxidize several days after manufacture. To investigate if this had any effect on sensor performance, indentation experiments were repeated with the same sensor with stress intensifiers on days 9 and 16 after manufacture. As shown in the figure, sensor sensitivity does not change significantly over this period.

IV. Experimental Evaluation of Sensing Skin for Neurosurgical Endoscope

To evaluate use as a cylindrical sensing skin, a 3×3 sensor array was fabricated that incorporated stress concentration features for all sensors as shown in Fig. 11(a). Using the technique of Fig. 4, the array was rolled around a polyimide tube (American Durafilm Co., Inc., Holliston, MA), which served as the backing layer. The seam was sealed with PDMS and rolled tightly in a 125μm thick PTFE sheet. Once the PDMS had cured, the PTFE sheet was removed leaving a 0.8mm thick cylindrical sensing skin. In this configuration, it is easily slipped on and off a standard 6.5mm neuroendoscope (Fig. 11(b)).

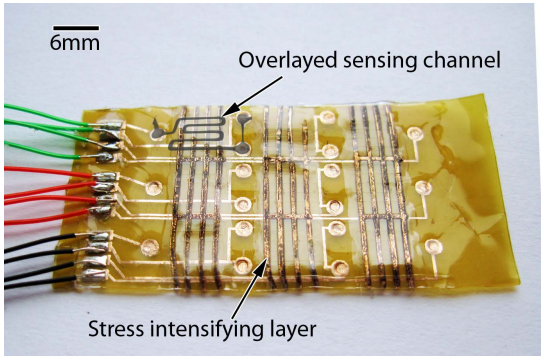

(a)

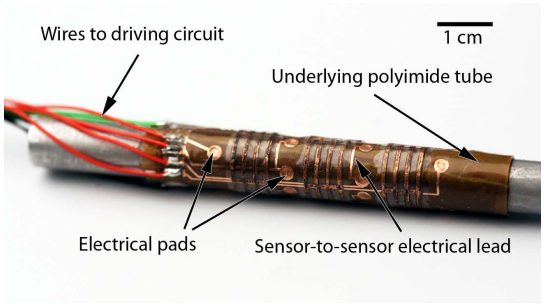

(b)

Fig. 11. Sensor array. (a) Planar configuration. (b) Cylindrical configuration positioned on 6.5mm diameter tube for testing.

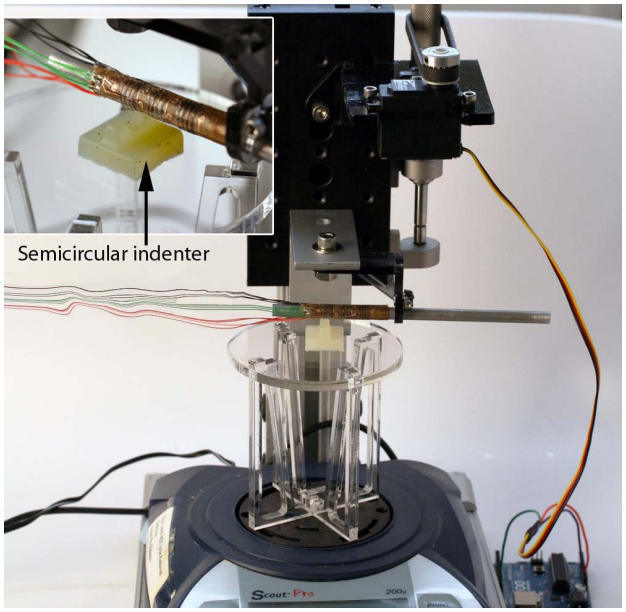

Fig. 12. Automated test setup for sensor evaluation.

A. Testing Procedure

Automated testing of the resulting sensing skin was performed as shown in Fig. 12. As shown in the inset, the indenter shape for these tests consisted of a half cylinder cutout with a diameter of 6.5mm and a length of 5mm. Two indenters were tested. The first, fabricated from a stiff acrylic with Young's modulus of 3.2×10^9GPa, was designed to produce the maximum sensor response for a given applied load. The second indenter was fabricated from Ecoflex 00-50 rubber (Smooth-On, Easton, PA). With Shore A scale hardness

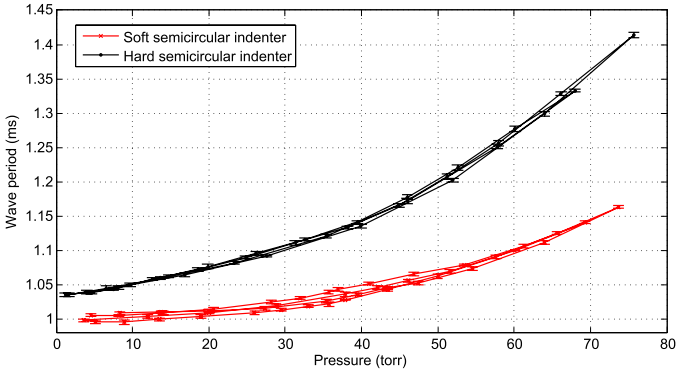

Fig. 13. Comparison of glycerol-based sensor response for acrylic and rubber indenters. Two loading/unloading trials are shown for each indenter.

of ∼5 and a Young's modulus of 0.26MPa , it approximates the stiffness of cortical tissue [27]. The semicircular shape ensures full and uniform contact of the sensing skin with the indenter surface, mimicking clinical contact with brain tissue.

In order to capture any hysteresis, the applied force was increased in steps from the minimum to the maximum value and then stepped back down to the minimum value. Three trials of each experiment were performed. Conversion of force to pressure assumed that total force wass uniformly distributed over the area of contact, defined as: $A = \pi RL$, where $R = 3.25$mm is the radius of the introducer sheath, and $L = 5$mm is the length of the indentation surface, thus yielding $A = 51\text{mm}^2$. The contact pressure is calculated as $P = F/A$, where F is the weight measured by the scale.

B. Experiments

Two types of experiments were performed to characterize the performance of the sensor array. The first compares the response obtained with the stiff and compliant indenters. The second compares the responses of the previously reported eGaIn sensor array with the newly proposed salt-saturated glycerol array for the range of pressures encountered in neurosurgical endoscopy (0-60torr). Each is described below.

1) Hard Versus Soft Indenter: It can be anticipated that a stiffer indenter will induce more deformation in the sensing channels than a softer indenter since the load it transmits will be more localized. While we are most interested in calibrating the sensor response for a given tissue stiffness, it is of interest to measure the response to a very stiff indenter since this provides an upper bound on force sensitivity.

The responses to semicylindrical indenters made of a stiff acrylic and a rubber matched to the stiffness of cortical tissue are compared in Fig. 13. As anticipated, the hard indenter produces a larger response. This comparison makes it clear that the pressure sensor array has to be calibrated for the tissue with which it is intended to be used in order to get accurate pressure measurements. Note that many types of soft sensor are likely to exhibit similar behavior. One way to perform this calibration would involve molding an indenter with the desired tissue stiffness and collecting load data as described in the paper.

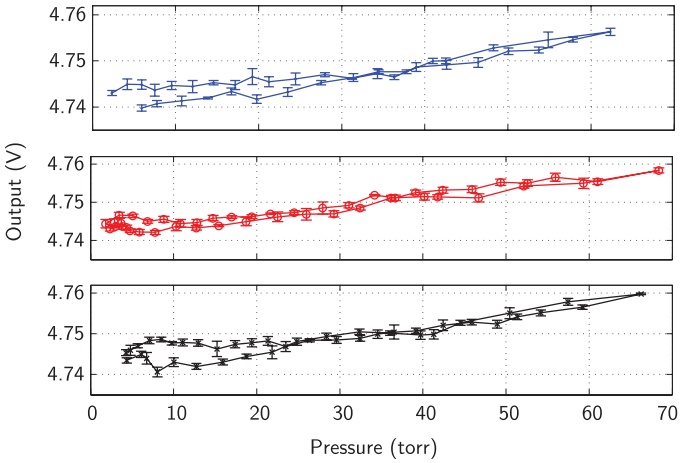

Fig. 14. eGaIn sensor testing showing three loading/unloading trials of a sensor.

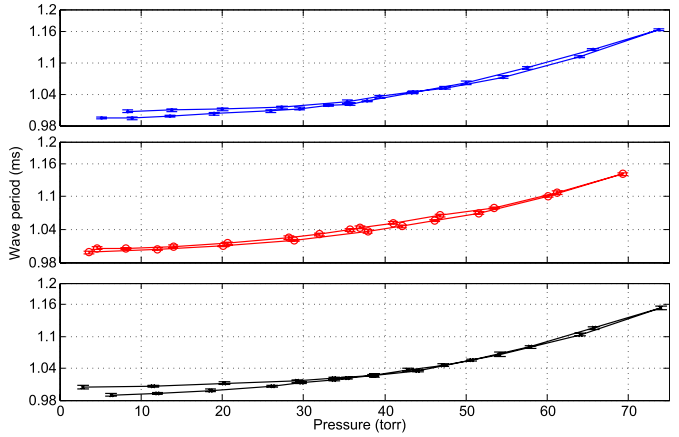

Fig. 15. Glycerol sensor testing showing three loading/unloading trials of a sensor.

2) Salt-Saturated Glycerol Versus eGaIn Sensors: Brain tissue is among the most sensitive in the human body and the range of pressures for neuroendoscopic sensing is 0-60torr [24]. To provide a baseline against which to compare the proposed biocompatible sensors, new experiments were conducted using the eGaIn sensor array of Fig. 1 which was fabricated as described in our prior work [24].

Using the eGaIn sensor array of Fig. 1 and the salt and glycerol array of Fig. 11, three trials were performed using the soft indenter on a single sensor of each array. The experimental responses appear in Figs. 14 and 15, respectively. Note that since the eGaIn sensors are excited with a DC voltage, their output resistance is measured as a voltage. Thus, it is not possible to directly compare their voltage output with the wave period output of the AC-excited salt and glycerol sensors.

Since minimal hysteresis is observed for either sensor over this pressure range, the data points of the three trials were combined for analysis as shown in Figs. 16 and 17. To facilitate comparison of the sensors which have different output units (volts versus wave period), the axes have been interchanged in these plots so that the sensor output signal

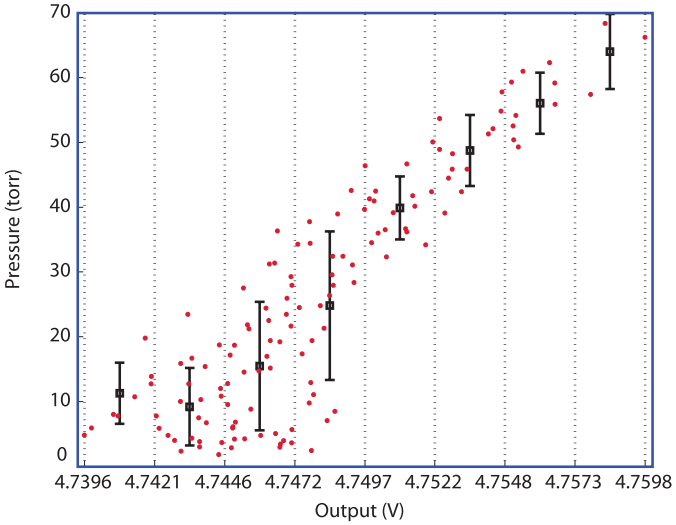

Fig. 16. eGaIn sensor data. Dashed vertical lines indicate boundaries of data bins used to compute labeled bin averages and standard deviations.

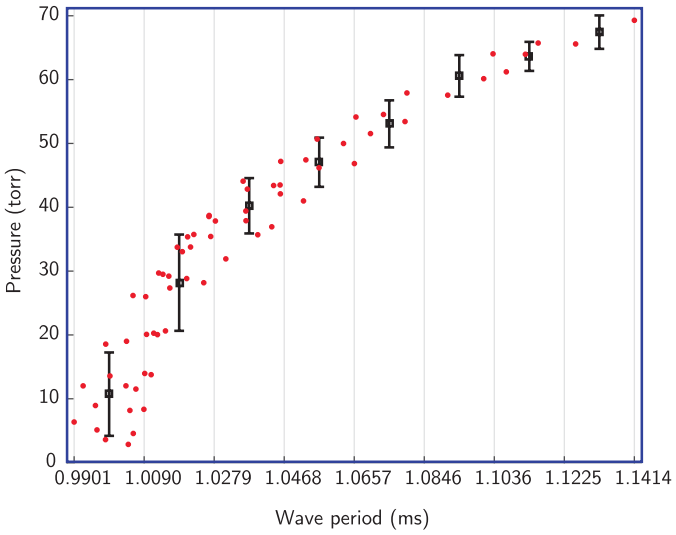

Fig. 17. Glycerol sensor data. Dashed vertical lines indicate boundaries of data bins used to compute labeled bin averages and standard deviations.

appears on the horizontal axis and pressure appears on the vertical axis.

Both sensors fail to accurately measure pressure below a minimum pressure value. For the eGaIn sensor, this minimum value is about 30torr while for the glycerol sensor, the minimum value is about 20torr. This corresponds to the minimum pressure needed to deform the channels sufficiently to produce a signal change exceeding the noise level. To provide a comparison of the variation in pressure associated with sensor output values, the output data for each sensor was divided into eight bins of equal width as shown in the figures. The mean and standard deviation of the points in each bin are shown in the figures.

It is observed that, for most bins, the glycerol and salt sensor produces a smaller standard deviation of pressure than the eGaIn sensor. To consider this in detail, the coefficient of variation, computed as the ratio of standard deviation to mean

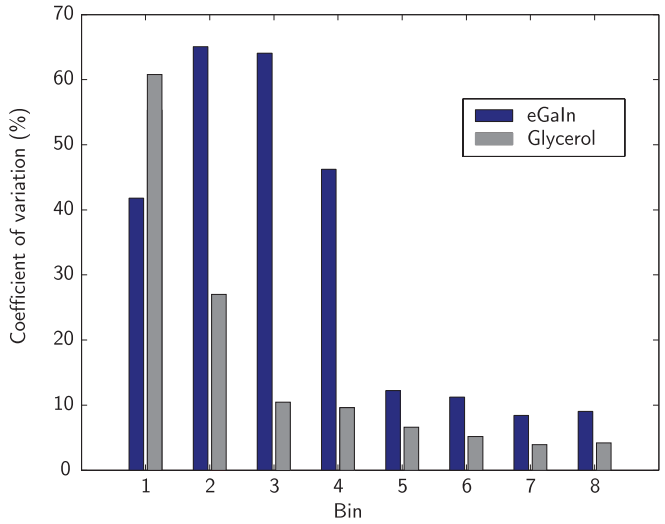

Fig. 18. Coefficient of variation for salt-saturated glycerol and eGaIn sensors versus data bin.

for each data bin, is plotted in Fig. 18. The bins are numbered from left to right. The eGaIn-filled sensor exhibits a coefficient of variation of 40% or more for the first four bins and drops below 10% only for bins 7 and 8. In contrast, the coefficient of variation of the glycerol-filled sensor falls to 11% in the third bin, falls below 10% in bin 4 and decreases monotonically to 4% in bin 8. In summary, the glycerol-filled sensor is able to provide accurate measurements starting at lower pressures and also provides both better and increasing accuracy at higher pressures.

V. Conclusion

Pressure-sensing skins that can be slipped over endoscopes and other interventional tools are an enabling technology that could spur the creation of a new generation of smart instruments. The simplest such implementation is to provide a display (e.g., visual) that alerts the clinician when dangerous pressures are applied, as illustrated in [24]. When used with robotic endoscopes and catheters, however, sophisticated control strategies become possible. For example, such sensor arrays can be integrated to create a co-robotic controller through which motion control is shared between the clinician and the robot. For example, the clinician could actively control the tip position while the controller autonomously adjusts the configuration of the robot to minimize tissue contact forces applied along its length.

This paper has demonstrated a promising new approach to producing cylindrical arrays of pressure sensors that are biocompatible and less than 1mm thick. The technology is inexpensive to manufacture since it uses a simple multi-layer manufacturing paradigm and also uses inexpensive electronics for signal interrogation.

By using a glycerol-based ionic solution, evaporation problems were avoided. While initial tests using aqueous ionic solutions exhibited visible evaporation from the channels within several days rendering the sensors inoperable, the glycerol-based solution displayed no signs of evaporation over multiple weeks of testing.

In comparison to prior eGaIn designs, measurement range and accuracy are improved. This may be due to the layer of stress concentration features introduced in the proposed design to boost sensitivity. Future work will consider optimizing the geometry of these features, such as, their cross section, pattern and intersection points with the sensing channels.

There are a variety of improvements that can be made to the current sensor design to enhance stretchability and flexibility and so facilitate its use on flexing instruments such as steerable endoscopes and catheters. The stiffest components are the Kapton-backed flex circuit and the stress intensifying copper layer. The Kapton can be replaced by a flexible insulating polymer while a conductive polymer could be used in place of the copper traces [28]. Stretchability of the copper stress intensifying layer could be enhanced by replacing the connected pattern with discrete intensifiers positioned under the conductive channels. Alternately, a stiff, but still stretchable polymer could be substituted for the copper, but with some loss of sensitivity due to the reduction in stiffness.

Ultimately, printing technologies that enable the deposition of sensors and electronics on flexible substrates could prove to be the most cost effective means of manufacturing the proposed sensors [28]. While current printing techniques are focused on solid phase materials, future methods may provide the means to fabricate sensors of type demonstrated here that include both solid and liquid components.

REFERENCES

[1] C. K. Rowe *et al.*, "A comparative direct cost analysis of pediatric urologic robot-assisted laparoscopic surgery versus open surgery: Could robot-assisted surgery be less expensive?" *J. Endourol.*, vol. 26, no. 7, pp. 871–877, 2012.

[2] A. Trejos, R. Patel, and M. Naish, "Force sensing and its application in minimally invasive surgery and therapy: A survey," *Proc. Inst. Mech. Eng. C, J. Mech. Eng. Sci.*, vol. 224, no. 7, pp. 1435–1454, 2010.

[3] P. Puangmali, K. Althoefer, L. D. Seneviratne, D. Murphy, and P. Dasgupta, "State-of-the-art in force and tactile sensing for minimally invasive surgery," *IEEE Sensors J.*, vol. 8, no. 4, pp. 371–381, Apr. 2008.

[4] M. I. Tiwana, S. J. Redmond, and N. H. Lovell, "A review of tactile sensing technologies with applications in biomedical engineering," *Sens. Actuators A, Phys.*, vol. 179, pp. 17–31, Jun. 2012.

[5] I. E. Araci, B. Su, S. R. Quake, and Y. Mandel, "An implantable microfluidic device for self-monitoring of intraocular pressure," *Nature Med.*, vol. 20, pp. 1074–1078, Aug. 2014.

[6] L. Y. Chen *et al.*, "Continuous wireless pressure monitoring and mapping with ultra-small passive sensors for health monitoring and critical care," *Nature Commun.*, vol. 5, p. 5028, Oct. 2014.

[7] P.-J. Chen, D. C. Rodger, S. Saati, M. S. Humayun, and Y.-C. Tai, "Microfabricated implantable parylene-based wireless passive intraocular pressure sensors," *J. Microelectromech. Syst.*, vol. 17, no. 6, pp. 1342–1351, Dec. 2008.

[8] A. Charalambides and S. Bergbreiter, "All-elastomer in-plane MEMS capacitive tactile sensor for normal force detection," in *Proc. IEEE SENSORS*, Nov. 2013, pp. 1–4.

[9] Z. Zhang *et al.*, "Experimental and theoretical studies of serpentine microstructures bonded to prestrained elastomers for stretchable electronics," *Adv. Funct. Mater.*, vol. 24, no. 14, pp. 2028–2037, Apr. 2014.

[10] T. Someya, T. Sekitani, S. Iba, Y. Kato, H. Kawaguchi, and T. Sakurai, "A large-area, flexible pressure sensor matrix with organic field-effect transistors for artificial skin applications," *Proc. Nat. Acad. Sci. USA*, vol. 101, no. 27, pp. 9966–9970, 2004.

[11] C. Pan *et al.*, "High-resolution electroluminescent imaging of pressure distribution using a piezoelectric nanowire LED array," *Nature Photon.*, vol. 7, pp. 752–758, Aug. 2013.

[12] X. Wang *et al.*, "Dynamic pressure mapping of personalized handwriting by a flexible sensor matrix based on the mechanoluminescence process," *Adv. Mater.*, vol. 27, no. 14, pp. 2324–2331, Apr. 2015.

[13] C. Lee, L. Jug, and E. Meng, "High strain biocompatible polydimethylsiloxane-based conductive graphene and multiwalled carbon nanotube nanocomposite strain sensors," *Appl. Phys. Lett.*, vol. 102, no. 18, pp. 183511–183516, 2013.

[14] C. Majidi, Y.-L. Park, R. Kramer, P. Bérard, and R. J. Wood, "Hyperelastic pressure sensing with a liquid-embedded elastomer," *J. Micromech. Microeng.*, vol. 20, no. 12, p. 125029, 2010.

[15] R. K. Kramer, C. Majidi, and R. J. Wood, "Wearable tactile keypad with stretchable artificial skin," in *Proc. IEEE Int. Conf. Robot. Autom.*, May 2011, pp. 1103–1107.

[16] A. H. Gosline, V. Arabagi, A. Kassam, and P. E. Dupont, "Achieving biocompatibility in soft sensors for surgical robots," in *Proc. Hamlyn Symp. Med. Robot.*, 2013, pp. 5–6.

[17] C.-Y. Wu, W.-H. Liao, and Y.-C. Tung, "Integrated ionic liquid-based electrofluidic circuits for pressure sensing within polydimethylsiloxane microfluidic systems," *Lab Chip*, vol. 11, no. 10, pp. 1740–1746, Mar. 2011.

[18] Y.-N. Cheung, Y. Zhu, C.-H. Cheng, C. Chao, and W. W.-F. Leung, "A novel fluidic strain sensor for large strain measurement," *Sens. Actuators A, Phys.*, vol. 147, no. 2, pp. 401–408, Oct. 2008.

[19] J.-B. Chossat, Y.-L. Park, R. J. Wood, and V. Duchaine, "A soft strain sensor based on ionic and metal liquids," *IEEE Sensors J.*, vol. 13, no. 9, pp. 3405–3414, Sep. 2013.

[20] M. A. Eddings and B. K. Gale, "A PDMS-based gas permeation pump for on-chip fluid handling in microfluidic devices," *J. Micromech. Microeng.*, vol. 16, no. 11, pp. 2396–2402, 2006.

[21] C. Majidi, R. Kramer, and R. J. Wood, "A non-differential elastomer curvature sensor for softer-than-skin electronics," *Smart Mater. Struct.*, vol. 20, no. 10, p. 105017, 2011.

[22] D. M. Vogt, Y.-L. Park, and R. J. Wood, "Design and characterization of a soft multi-axis force sensor using embedded microfluidic channels," *IEEE Sensors J.*, vol. 13, no. 10, pp. 4056–4064, Oct. 2013.

[23] R. Tan, P. Benharash, P. Schulam, and J. J. Schmidt, "Implantable electrolyte conductance-based pressure sensing catheter, II. Device construction and testing," *Biomed. Microdevices*, vol. 15, no. 6, pp. 1035–1041, Dec. 2013.

[24] P. J. Codd, V. Arabagi, A. H. Gosline, and P. Dupont, "Novel pressure-sensing skin for detecting impending tissue damage during neuroendoscopy," *J. Neurosurgery, Pediatrics*, vol. 13, no. 1, pp. 114–121, Jan. 2014.

[25] Y. H. Lei, Y. P. Liu, W. Wang, W. G. Wu, and Z. H. Li, "Fabrication and characterization of parylene C-caulked PDMS for low-permeable microfluidics," in *Proc. Micro Electro Mech. Syst. Conf.*, Jan. 2011, pp. 1123–1126.

[26] Y. Mengüç *et al.*, "Soft wearable motion sensing suit for lower limb biomechanics measurements," in *Proc. IEEE Int. Conf. Robot. Autom.*, May 2013, pp. 5289–5296.

[27] D. A. Hudson, "Medical procedures training model," U.S. Patent 8 105 089, Jan. 31, 2012.

[28] S. Khan, L. Lorenzelli, and R. S. Dahiya, "Technologies for printing sensors and electronics over large flexible substrates: A review," *IEEE Sensors J.*, vol. 15, no. 6, pp. 3164–3185, Jun. 2015.

Veaceslav Arabagi received the M.S. and Ph.D. degrees in mechanical engineering from Carnegie Mellon University, in 2009 and 2011, respectively. He was a Post-Doctoral Researcher with Boston Children's Hospital, working in the fields of medical robotics, soft sensing, and actuation. He is currently developing medical devices with Helbling Precision Engineering.

Ouajdi Felfoul received the M.S. and Ph.D. degrees in biomedical engineering from Polytechnique Montreal, Canada, in 2005 and 2011, respectively. He was a Post-Doctoral Research Fellow with the Pediatric Cardiac Bioengineering Laboratory, Boston Children's Hospital, where his research centered on developing robotic technology that is powered, controlled, and imaged by magnetic resonance imaging (MRI) systems. He currently develops MRI technology for GE Healthcare.

Andrew H. Gosline (M'03) received the M.A.Sc. degree in electrical engineering from the University of British Columbia, and the Ph.D. degree in electrical engineering from McGill University. His academic research focused on medical robotics, applied control, surgical simulation, and mechatronic device development. He is currently the Principal Engineer with Human Design Medical LLC, a respiratory device company that develops portable xPAP devices and accessories.

Robert J. Wood (M'01) received the M.S. and Ph.D. degrees from the Department of Electrical Engineering and Computer Sciences, University of California, Berkeley, in 2001 and 2004, respectively. He is currently the Charles River Professor of Engineering and Applied Sciences with the Harvard John A. Paulson School of Engineering and Applied Sciences, a Founding Core Faculty Member of the Wyss Institute for Biologically Inspired Engineering, Harvard University, and a National Geographic Explorer. His current research interests include microrobotics, soft and wearable robots, and bioinspired robotics.

Pierre E. Dupont (M'99–SM'03–F'11) received the B.S., M.S., and Ph.D. degrees in mechanical engineering from the Rensselaer Polytechnic Institute, Troy, NY, in 1982, 1984, and 1988, respectively. From 1988 to 1990, he was a Post-Doctoral Fellow with the School of Engineering and Applied Sciences, Harvard University, Cambridge, MA. He was a Professor of Mechanical Engineering and Biomedical Engineering with Boston University, Boston, MA. He is currently the Chief of Pediatric Cardiac Bioengineering and holder of the Edward P. Marram Chair at Boston Children's Hospital, Harvard Medical School, Boston, where he is engaged in developing instrumentation and imaging technology for minimally invasive surgery.